A Curvature-Enhanced Random Walker Segmentation Method For Detailed Capture of 3D Cell Surface Membranes

E. Josiah Lutton
josiah.lutton@warwick.ac.uk
Sharon Collier
s.collier.3@warwick.ac.uk
Till Bretschneider
t.bretschneider@warwick.ac.uk

Department of Computer Science
University of Warwick
Coventry, UK

Abstract

High-resolution 3D microscopy is a fast advancing field and requires new techniques in image analysis to handle these new datasets. In this work, we focus on detailed 3D segmentation of *Dictyostelium* cells undergoing macropinocytosis captured on an iSPIM microscope. We propose a novel random walker-based method with a curvature-based enhancement term, with the aim of capturing fine protrusions, such as filopodia and deep invaginations, such as macropinocytotic cups, on the cell surface. We tested our method on both real and synthetic data, demonstrating that the inclusion of the curvature enhancement term can improve the segmentation of the aforementioned features. We show that our method performs better than the random walker and power watershed in real and synthetic data, and that our method performs better than the random forest pixel classifier in real data. We also present an automated seeding method for microscopy data, which, combined with the curvature-enhanced random walker method, enables the rapid segmentation of large time series with minimal input from the experimenter.

1 Introduction

Recent advances in 3D microscopy have enabled the detailed capture of large time series of cells, posing challenges of accurately segmenting them in high resolution. In this work we focus on the segmentation of *Dictyostelium* cells undergoing macropinocytosis. Macropinocytosis is the uptake of extracellular fluid employed in important biological processes, including antigen processing and cancer cell feeding [26]. It involves the formation of highly concave regions of the cell membrane, macropinocytotic cups. The cells also contain filopodia, which are fine protrusions on the cell membrane, acting as cellular sensors. The aim of the segmentation method proposed here is to accurately capture these detailed structures. The cells examined expressed LifeAct-GFP, a commonly used fluorescent F-actin marker, which produced high intensity signals in both of these features. Light sheet imaging of macropinocytosis has gained recent interest [9]. Accurate segmentation of the structures involved in macropinocytosis is required to better understand this process [8, 36].

Our segmentation method is based on the random walker segmentation, a standard method for segmenting objects in 2- and 3-dimensional images [13, 20]. In practice, images always suffer from a remaining degree of blurring, because deconvolution hardly ever achieves

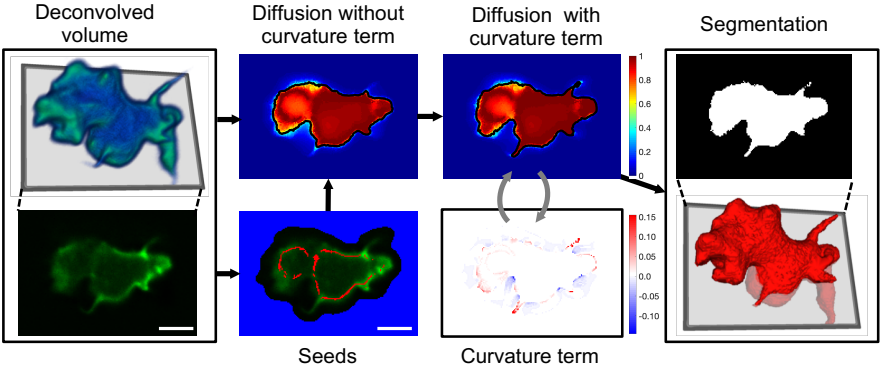

Figure 1: Flow chart outlining the major steps in the segmentation algorithm. *Dictyostelium* cells expressing LifeAct-GFP were imaged on an iSPIM microscope, as described in Section 5.4. 3D image pseudocoloured by intensity (blue represents low intensity, green represents high). Automatic seed selection for foreground (red) and background (blue) is based on Phansalkar thresholding [29], as described in Section 4. The random walker method is implemented by simulating diffusion until equilibrium was reached, using the automatically selected seeds and image gradient-based weighting, as described in section 3. Diffusion with an additional curvature term is subsequently simulated, with the same inputs as before, using the equilibrium values of the previous simulation as initial conditions, as described in Section 3. Contour lines show the location of the 0.5 isosurface, which corresponds to the segmentation boundary. The curvature term is dependent on the diffusion system, and is periodically updated and fed back into the diffusion system. The curvature term is constructed to be strongest close to the segmentation boundary, and restricted to negative values outside this boundary and positive values inside. Scale bars represent 5 μm.

theoretically optimum deblurring, compromising fine protrusions and invaginations more strongly than moderately curved structures. This blurring causes protrusions to be truncated or lost during segmentation, while invaginations tend to lose depth. We propose a novel random walker-based method that uses a curvature enhancement term to recover these structures. Additionally, we present a method for automated seed selection for the random walker, which utilises the fluorescence pattern of the F-Actin marker. These methods were tested on both real and synthetic data, showing that the addition of curvature enhancement to the random walker method can provide a marked improvement in the segmentation of detailed structures such as those mentioned above. We compared our method with two state of the art segmentation methods: the power watershed and the random forest pixel classifier, and show that our method outperforms both in real data.

2 Related Work

The random walker is a commonly-used method of supervised image segmentation [13, 20]. This method is part of a broader family [10, 33] of graph-based segmentation methods, which includes graph cuts [5] and watersheds [4]. These methods model the image as a graph $G = (V, E)$ where the vertices $V = \{v_i\}$ corresponding to image pixels and

edges $E = \{e_{ij}\}$ corresponding to the adjacency relationship of the pixels, with e_{ij} representing the edge between v_i and v_j. For a given edge weighting $W = \{w_{ij}\}$, the aim of a graph-based segmentation is to find a function x on G that minimizes an energy term of the form [10]

$$\sum_{e_{ij} \in E} w_{ij}^p |x_i - x_j|^q, \tag{1}$$

where $x_i = x(v_i)$, $x_i = 1$ at foreground seeds, and $x_i = 0$ at background seeds. The segmented foreground is given by points with $x > 0.5$. The choice of q and p determine which segmentation method is being used: $q = p = 1$ corresponds to graph cuts [33]; $q = p = 2$ corresponds to the random walker [33]; $q = p \to \infty$ corresponds to shortest paths [33]; $q = 1, p \to \infty$ corresponds to the watershed [1, 10]; and $q > 1, p \to \infty$ corresponds to the recently-developed power watershed [10]. Extensions to these methods include adding prior information to the energy function [13, 19], the addition of auxiliary nodes [11, 22], and modification of the edge weighting w_{ij} [28, 38], which is typically based on image gradients.

Curvature was used previously by M'hiri *et al.* [28] in the weighting of the random walker in order to enhance segmentation of blood vessels. This method was facilitated by using a measure of "vesselness" [17] in the input image to inform the weighting of the system. This method is not readily applicable to segmenting individual cells, since the structures of interest do not necessarily conform to an easily-defined shape. Another use of curvature in vessel segmentation is in a regularization term for the fast marching segmentation algorithm [25], with the aim of avoiding high-curvature surfaces.

Our methods utilise a model of the random walker based on the discretisation of an anisotropic diffusion system [20, 37]. This model allows the addition of a mean curvature term to the model equation. Applications of mean curvature flow in image analysis include image enhancement [2, 27] and active contour-based segmentation methods [7, 21, 32]. An example that is closely related to the present work is a method of image enhancement proposed by Malladi and Sethian [27], which uses a function of curvature that takes on positive or negative values of curvature depending on the local image properties. This function is similar in construction to the curvature term in Eq. 7 below. Related to mean curvature flow is Willmore flow [24], which has also been used in level set segmentation methods [12]. In 2D systems the Willmore flow is equivalent to minimization of Euler's elastica energy [16], which has previously been employed in the weighting of graph cut segmentation [14, 15]. These curvature-based segmentation methods use curvature to stabilize the boundaries of segmentation, which is the reverse of the effect produced by the methods presented here; we employ a term that effectively reverses the flow of curvature to improve the segmentation of protrusions and invaginations.

The random walker is highly dependent on the initial seeding [14]. Previous implementations of the random walker algorithm have used manual [20], semi-automated [13], and fully-automated seed selection [34]. Here we present an automated method of seed selection based on Phansalkar thresholding [29].

3 The curvature-enhanced random walker method

Random walker segmentation can be modelled as the steady state of a discretisation of the anisotropic diffusion system [20, 37]:

$$\frac{\partial v}{\partial t} = \nabla(W \nabla v), \tag{2}$$

subject to the constraints

$$v(x,t) = 1 \text{ if } x \in FG, \tag{3}$$

$$v(x,t) = 0 \text{ if } x \in BG, \tag{4}$$

where FG and BG are the sets of foreground and background pixels, respectively, and W is the diffusion weighting function, defined discretely for between two pixels x and y, as

$$W(x,y) = \exp(-\beta||I(x)-I(y)||^2 - \alpha(||x-y||^2)/W_{\max}, \tag{5}$$

where $||.||$ is the Euclidean norm, $I(x)$ and $I(y)$ are the input image intensities at x and y respectively, $W_{\max} = \exp(-\alpha)$ is a normalization constant, and β and α are parameters to be fixed. We set $\alpha = \beta/255^2$ in accordance with previous work by Du *et al.* [13] (scaling by 255^2 accounts for the $[0,255]$ normalization used in [13]). Weights are computed for 18-connected neighbourhoods. The discretised form of Eq. 2 for the point x is

$$(v(x,t+dt) - v(x,t))/dt = \sum_{y \in N(x)} W(x,y)(v(y,t) - v(x,t)), \tag{6}$$

Where $N(x)$ is the 18-connected neighbourhood of x. The equilibrium values of v are computed using the forward Euler method, with the segmentation (in the absence of curvature enhancement) given by pixels with $v > 0.5$ [37].

The curvature-enhanced random walker is defined by the system

$$\frac{\partial v}{\partial t} = \nabla(W\nabla v) + \kappa\tilde{H}(v)v(1-v), \tag{7}$$

subject to constraints 3 and 4, where κ is a fixed parameter, W is as defined in Eq. 5, and

$$\tilde{H}(v) = \begin{cases} H(v) & \text{if } H(v)(v-0.5) > 0 \\ 0 & \text{otherwise} \end{cases} \tag{8}$$

where

$$H(v) = -\nabla \cdot \frac{\nabla v}{||\nabla v||} \tag{9}$$

is the mean curvature. As with the standard random walker, equilibrium values of v are calculated and the segmentation is given by pixels with $v > 0.5$.

The gradients in 9 are approximated in each direction using an extension of the 3D Sobel filter, which is given in the x-direction as a smoothing in y and z by applying the 1D filter $(1,4,6,4,1)/16$ in both y- and z-directions, Followed by a differencing filter in x with radius 3, given by $(-1,0,0,0,0,0,1)/6$. The formulation for y- and z-directions are defined similarly. The expanded smoothing radius is required because the divergence of the normal directions is highly sensitive to noise. The differences are taken at a distance of 3 to reduce sensitivity to small fluctuations in the shape of the isosurface. The number of operations involved in this computation are much higher than for the finite differences in the random walker, and therefore increase computation time. In our implementation we were able to improve the speed by only computing the curvature every 10 time steps, which had a negligible impact on the resulting segmentation.

The curvature-enhanced random walker segmentation is implemented on a GPU as follows. Initially, the equilibrium values v_1 of the standard random walker system are computed,

with initial conditions $v(x,0) = 0.5$ for all x not in either of the seed sets. The equilibrium values v_2 of the curvature-enhanced diffusion system are subsequently computed with initial conditions $v(x,0) = v_1$. The segmentation is given by the set of pixels with $v_2 > 0.5$. Note that, for large values of κ, this system becomes unstable and equilibrium is not reached. In these cases, simulations are terminated after a fixed number of time steps.

4 Seed selection

Automated seed selection is performed on microscopy data based on the Phansalkar threshold [29]. The Phansalkar threshold T at a point x is given by

$$T(x) = \mu(x)(1 + p\exp(-q\mu(x)) + k(\sigma(x)/r - 1)), \tag{10}$$

where $\mu(x)$ and $\sigma(x)$ are the local mean and standard deviation of the image intensity, and p, q, k, and r are fixed parameters. The value of p is set to 2, and the local neighbourhood for calculating $\mu(x)$ and $\sigma(x)$ is given by a cube of side 21 pixels centred at x. The values of q, k, and r are found based on each individual image. The value of q is set so that the exponential decays by half over two standard deviations of the local means:

$$q = \log(2)/(2\sigma_\mu), \tag{11}$$

where σ_μ is the standard deviation of all local mean values in the image. The values of r and k are set based on the following assumptions. Foreground pixels are assumed to have local standard deviation equal to the maximum local standard deviation $\hat{\sigma}$, which maximizes T in Eq. 10, and local mean

$$\mu_{FG} = \mu_\mu + 2\sigma_\mu, \tag{12}$$

where μ_μ is the mean of all local means in the image, and σ_μ is as in Eq. 11. Conversely, background pixels are assumed to have zero local standard deviation (minimizing T in Eq. 10) and local mean

$$\mu_{BG} = \mu_\mu + \sigma_\mu, \tag{13}$$

where μ_μ and σ_μ are as above. We define r and k based on these assumptions:

$$r = \hat{\sigma}/(1 - \exp(-q(\mu_{FG} - \mu_{BG}))), \tag{14}$$

$$k = p(\exp(-q\mu_{BG}) + \exp(-q\mu_{FG})/(1 - \hat{\sigma}/r))/2. \tag{15}$$

These values ensure that any pixels conforming to the assumptions made on foreground pixels will have a threshold value below the local mean, while any pixels conforming to the assumptions made on background pixels will have a threshold value above the local mean. An example of the output of this thresholding is shown in Fig. 2B.

Background seeds are obtained by applying a spherical dilation operator of radius 10 pixels to the binary volume obtained by the Phansalkar thresholding, filling holes, applying a spherical erosion operator of radius 5, and inverting the resulting binary image. An example of the result of this process is shown in Fig. 2C.

Foreground seeds are selected to represent maximal surfaces in the image. Gradients are computed using a Sobel operator (Fig. 2D). Each pixel is assigned the direction of the

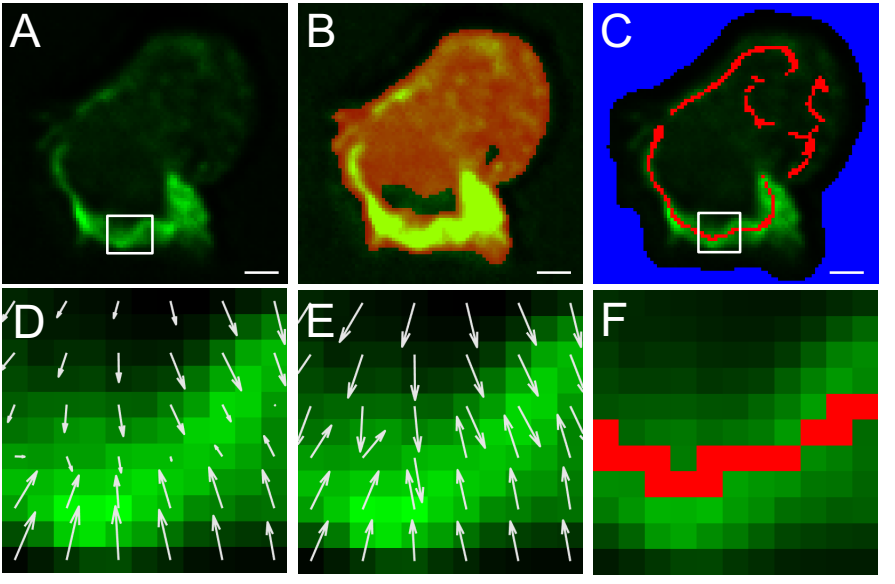

Figure 2: Automated seed selection. A: A slice through a volume to be segmented. White box indicates the position of D–F. B: The result of applying the Phansalkar threshold (red channel). C: Automatically selected background (blue) and foreground (red) seeds. White box indicates the position of F. Foreground seeds are obtained from the thresholded points according to D–F. D: Gradients, subsampled for ease of visualisation. Gradient magnitude is used to identify local maxima. E: Normalized maximal gradient directions, used to compare gradient magnitudes. F: Foreground seeds resulting from comparing gradient magnitudes (D) along the locally maximal gradient direction (E). Scale bars represent 2 μm.

largest magnitude gradient within a 26-connected neighbourhood for the purposes of comparison (Fig 2E). Magnitudes along the assigned direction are linearly interpolated from the neighbouring pixels, and a pixel is labelled as a turning point if its gradient magnitude is lower than these interpolated magnitudes. Turning points with a negative Laplacian are labelled maximal. This set of maximal points is restricted to points marked as foreground by the Phansalkar thresholding algorithm. To further improve the robustness of this algorithm, the maximal points are grouped into (6-)connected components. The largest connected component is labelled as foreground. Any other connected components larger than one pixel with mean intensity greater than the mean intensity of the largest connected component are also labelled as foreground. An example of the result of this process is shown in Fig. 2C.

5 Experiments and Results

We compared our method with other segmentation methods on both synthetic and real data. A localized form of the Jaccard score was used to evaluate the relationship between β and κ. This localized Jaccard score, along with the global Jaccard score, boundary displacement error, and Hausdorff score were used to compare all segmentation methods.

5.1 Evaluation methods

The measures used to evaluate the segmentation results were the Jaccard score, a localised form of the Jaccard score, the Hausdorff distance, and the mean boundary displacement error [18]. The first two measures describe how a segmentation performs on a pixel-wise basis, while the second two measures describe how the surface of the segmented shape differs from that of the ground truth.

For a ground truth image with foreground pixel set S_{GT} and segmented image with foreground pixel set S_{SEG}, the Jaccard score Jac for the segmentation is given as

$$Jac = \frac{|S_{GT} \cap S_{SEG}|}{|S_{GT} \cup S_{SEG}|}. \tag{16}$$

Here, we find it more informative to compare segmentations to ground truth in a localised fashion. For a point p with neighbourhood $N(p)$, the local Jaccard score Jac_{loc} is given as

$$Jac_{loc}(p) = \frac{|S_{GT} \cap S_{SEG} \cap N(p)|}{|(S_{GT} \cup S_{SEG}) \cap N(p)|}. \tag{17}$$

Because this measure is defined as a proportion of foreground pixels in a local neighbourhood, points with a neighbourhood populated with mostly foreground pixels will show less variation than a neighbourhood populated with mostly background pixels. To address this difference, we also take the local Jaccard score of the negative spaces:

$$Jac'_{loc}(p) = \frac{|(N(p) \setminus S_{GT}) \cap (N(p) \setminus S_{SEG})|}{|(N(p) \setminus S_{GT}) \cup (N(p) \setminus S_{SEG})|}. \tag{18}$$

The overall local Jaccard score is thus defined as the lowest of these two scores:

$$\hat{Jac}_{loc}(p) = \min(Jac_{loc}(p), Jac'_{loc}(p)). \tag{19}$$

For boundary difference measures, we first define the boundary of a shape in a binary image as the set of foreground pixels with at least one adjacent background pixel (26-connected). The distance from a point p to a boundary set B is given as

$$d(p,B) = min_{q \in B} ||p - q||, \tag{20}$$

where $||\cdot||$ is the Euclidean norm. For a ground truth boundary set B_{GT} and segmented boundary set B_{SEG}, the Hausdorff distance is given as

$$HD = max\{max_{p \in B_{GT}} d(p, B_{SEG}), max_{q \in B_{SEG}} d(q, B_{GT})\}. \tag{21}$$

The mean boundary displacement error (BDE) is an asymmetric measure of the distance between the surfaces. The mean BDE from B_{GT} to B_{SEG} is given as

$$BDE_{GT \to S} = \frac{1}{|B_{GT}|} \sum_{p \in B_{GT}} d(p, B_{SEG}). \tag{22}$$

The mean BDE from B_{SEG} to B_{GT} is similarly defined.

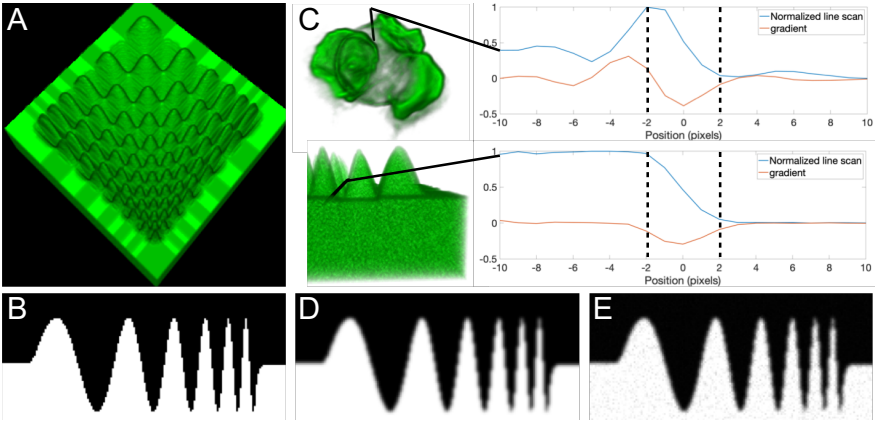

Figure 3: Synthetic data. A: Synthetic shape created to test the effectiveness of the curvature-enhanced random walker algorithm. B: Slice through the synthetic shape. C: Normalized line scans of real and synthetic data. Comparison of these line scans informed the choice of parameter values for Gaussian blurring (D) and applying Poisson noise (E).

5.2 Comparison to other methods

We compared the performance of our method with that of the random walker [20], the power watershed [10], and the random forest pixel classifier [6].

The random walker segmentation can be thought of as a special case of our method when $\kappa = 0$, and is automatically generated as the first step of our segmentation algorithm (see Section 3 and Fig. 1).

The power watershed is given by the energy optimization of Eq. 1 with finite q and $p \to \infty$ [10]. In the following, we use a value of $q = 2$ as used by Couprie *et al.* [10]. This method is also related to the random walker, in that it represents the limiting case of $\beta \to \infty$.

The random forest pixel classifier was implemented using the fast random forest method in the Trainable Weka Segmentation 3D plugin [6] for Fiji [51]. Because this pixel classifier determines foreground and background pixels based on local pixel data, the automated seeding developed for our segmentation method was inappropriate to use for training due to it selecting only local maxima as foreground. For this reason, we used random sampling of the ground truth foreground and background to train the classifier. We chose sampling rates N of 50 and 500 training samples per slide for our comparison; a rate of $N = 50$ samples per slide is comparable to the number of automatically selected foreground seeds in Section 4, while the higher rate of $N = 500$ was chosen to represent a highly fitted classifier. Once trained, the classifier was applied to the whole image to select foreground and background pixels. Based on preliminary testing, pixels were classified using the Gaussian, Hessian, and Laplacian features [6].

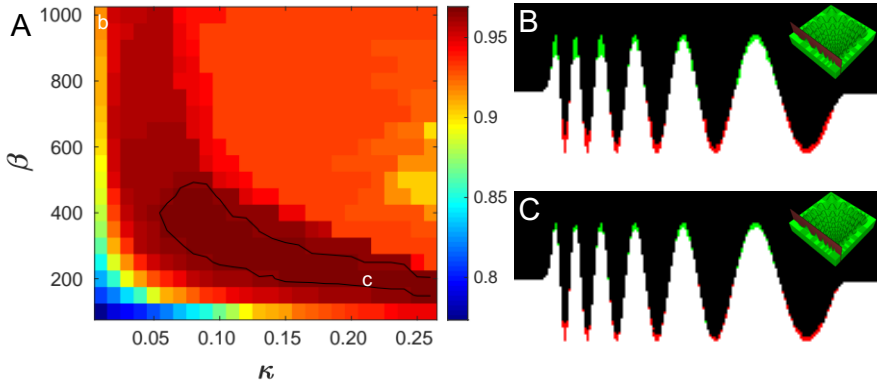

Figure 4: Results of experiments on synthetic data. A: Minimum local Jaccard scores (Eq. 17) for a range of parameter values. The optimal values of β and κ are negatively correlated, although even at high values of β a non-zero value of κ shows improvement on the standard random walker. Black contour line represents the 90th percentile. B: Comparison of the segmentation algorithm at point b (standard random walker) with the original mask. C: Comparison of the segmentation algorithm at point c (optimal values of β and κ) with the original mask. Red represents false positives, green represents false negatives, inset shows the position of the slice.

5.3 Synthetic data

5.3.1 Construction

Here we have chosen a shape with multiple protrusions and invaginations of varying widths (Fig. 3A). The resolution of the synthetic shape (Fig. 3B) was selected based on observation of microscopy data, such that the finest structures are only $1-2$ pixels wide. The intensity values were generated such that the shape boundaries have a similar pattern of intensities to that of real cells (Fig. 3C). The intensity pattern at a point on the manually identified boundary of a real cell was taken to be the pixel intensities along the line normal to the boundary. The pattern of intensities at the synthetic shape boundary was determined in the same manner. These line scans were normalized to $[0,1]$, so that the gradients at the boundary could be compared up to a scaling factor. The aim in the following is to match the distribution of the steepest gradients of these line scans in the synthetic data $\{g_s\}$ with that of the real data $\{g_r\}$. A Gaussian blur with standard deviation 1 was applied to the binary shape (Fig. 3D) so that the mean of $\{g_s\}$ (-0.31) is of a comparable to the mean of $\{g_r\}$ (-0.28). Poisson noise was subsequently applied to the blurred mask such that the standard deviation of $\{g_s\}$ (0.10) was comparable to the standard deviation of $\{g_t\}$ (0.09). Scaling the blurred image up by 500 and applying the Poisson noise achieved this effect. The resulting noisy image was normalized to $[0,1]$. The plane $z=0$ was taken as the foreground seed set (the bottom of the shape in Fig. 3A), while background seeds were taken to be the plane $z=80$ (above the shape in Fig. 3A).

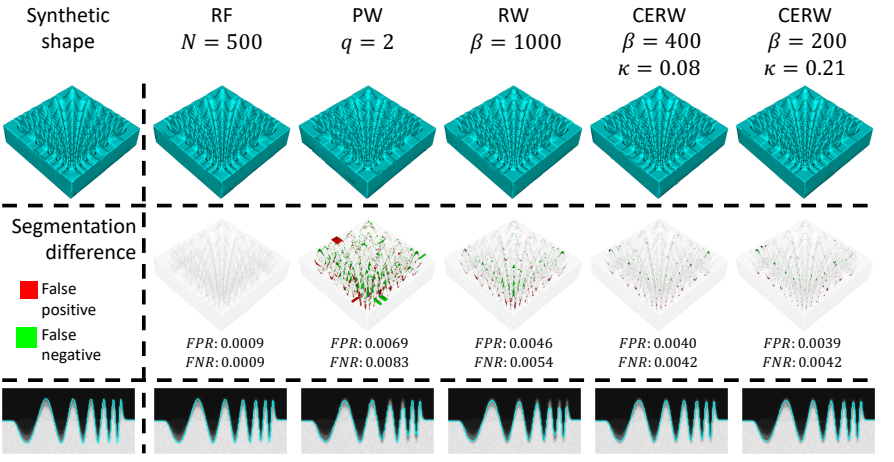

Figure 5: Comparison between the synthetic shape mask and random forest classifier (RF), power watershed (PW), random walker (RW), and curvature-enhanced random walker (CERW). Top row: synthetic shape surface (left) and surfaces generated by each segmentation method. Middle row: differences between segmentation results and the synthetic mask, where red marks false positive and green marks false negative. FPR: false positive rate, FNR: false negative rate. Bottom row: slices through each surface compared to the original image. While the RF clearly performs best, this is likely due to the synthetic nature of the image. The CERW outperforms both PW and RW, only showing small errors for both parameter sets.

5.3.2 Relationship between β and κ

The first experiment using this synthetic shape aims to investigate the relationship between β and κ in terms of segmentation performance. Here we use the localised Jaccard score, and use a neighbourhood of square cross-section (width 21) and depth equal to the depth of the stack (80 slices). This neighbourhood was constructed to include the full lengths of any protrusions or invaginations that intersect with the neighbourhood. Here we investigate the minimum local Jaccard score $J_{\min}$, which will highlight the score corresponding to the area of the shape where the segmentation performed the weakest. The results of this experiment are shown in Fig. 4. This shows that the values of β and κ that optimize the local Jaccard score are negatively correlated. Note that even for high values of β, the standard random walker can be improved with a relatively small value of κ.

5.3.3 Comparison with other methods

The broader set of segmentation methods are compared in Table 1 and Fig. 5. Unsurprisingly, the pixel classifier outperforms all other methods in this example, due to the fact that the image being analysed is directly based on a binary image. The curvature-enhanced random walker performs better than both the random walker and the power watershed in this example. The power watershed is particularly affected by the noise added to the image, as can be seen in the slice in Fig. 5. This noise sensitivity is avoided in the curvature-enhanced random walker because it enables the value of β to be reduced (compared to the optimal ran-

Method	JS	J_{min}	HD	BDE	
				S→GT	GT→S
RF (50)	0.9972	0.9793	6.00	0.0191	0.0439
RF (500)	**0.9982**	**0.9871**	**5.10**	**0.0122**	**0.0222**
PW (2)	0.9850	0.9222	8.54	0.1040	0.1943
RW (1000)	0.9900	0.9171	13.0	0.0646	0.1615
CERW (1000, 0.05)	0.9909	0.9586	13.0	0.0684	0.1130
CERW (400, 0.08)	0.9918	0.9685	*8.00*	0.0614	*0.1078*
CERW (200, 0.21)	*0.9920*	*0.9692*	*8.00*	*0.0608*	0.1082

Table 1: Comparison of segmentation methods applied to synthetic data. RF: random forest classifier, PW: power watershed, RW: random walker, CERW: curvature-enhanced random walker. Numbers in brackets are parameter values (see text for details). JS: Jaccard score, J_{min}: minimum local Jaccard score (see text for details), HD: Hausdorff distance, BDE: mean boundary displacement error, measuring the displacement of the ground truth (shape mask) boundary compared to the segmentation boundary (GT→S), and the reverse (S→GT). Bold numbers highlight the best value, italic numbers highlight the best non-classifier value (highest for Jaccard and minimum local Jaccard, lowest for Hausdorff distance and boundary displacement error).

dom walker), which reduces the impact of variable gradients between neighbouring pixels. Additionally, the curvature enhancement is able to compensate for the increased impact of blurring in the finer features, as can be seen in the slices in Fig. 5.

5.4 Microscopy data

5.4.1 Data acquisition and manual segmentation

The segmentation method described in Section 3, with seeds selected according to Section 4, was tested on 11 microscopy images that had been manually segmented for comparison. *Dictyostelium* cells expressing LifeAct-GFP were imaged on an inverted selective plane illumination microscope (iSPIM) [35]. The resulting images had pixel width 0.165 μm and slice thickness 0.2 μm. These images were deconvolved using the Richardson-Lucy algorithm [30]. The images selected for segmentation each contained a single cell undergoing macropinocytosis. Manual segmentations were drawn onto the 2D planes of the images, cycling through (x,y)- (x,z)-, and (y,z)- planes iteratively until a satisfactory segmentation was achieved. For computing the curvature-enhanced random walker segmentation, all microscopy images were normalized to $[0,1]$, and gamma correction (0.5) was applied.

5.4.2 Relationship between β and κ

As with the synthetic shape, we first evaluate how the segmentation is affected by the choice of β and κ. Here we use the localised Jaccard score with neighbourhood given by a cube of side 21 pixels, evaluated at all points on the manually segmented cell surface. It is of particular interest to evaluate the segmentation at points on the cell surface of highly positive and negative curvature, because these correspond to biologically significant features. We therefore separate points on the surface of the manually segmented cell into three sets: points with highly negative mean curvature ($H < -0.2$), highly positive mean curvature ($H > 0.2$),

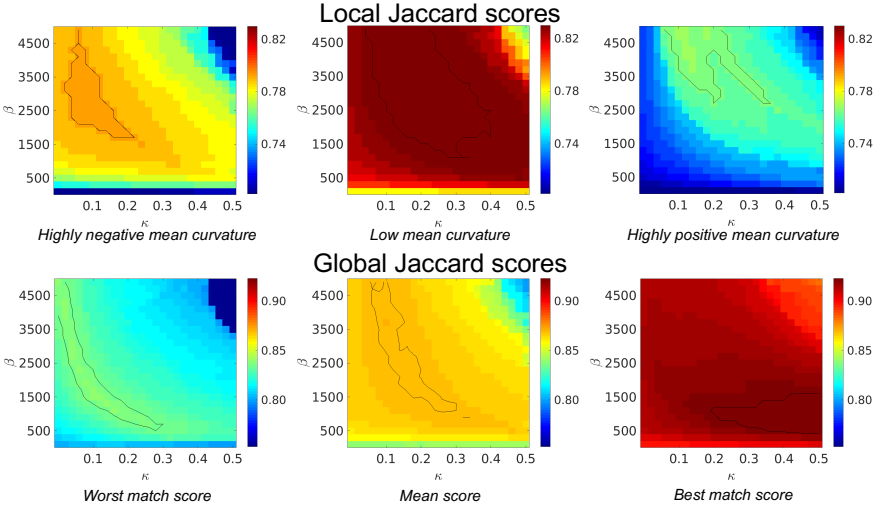

Figure 6: *Top row*: Mean local Jaccard scores for negative, low and positive curvatures of the surface of the manual segmentation of a cell, for a range of parameter values. As with the synthetic data, the optimal values of β and κ are negatively correlated. *Bottom row*: Minimum, mean, and maximum Jaccard scores for all segmented microscopy images for a range of parameter values. Again the negative correlation of the optimal values of β and κ is evident. Black contour lines represent the 90th percentile.

and points with low absolute curvature ($|H| \leq 0.2$). The mean local Jaccard scores for a range of β and κ values for each of these sets are summarized in the top row of Fig. 6. These images show a similar relationship between β and κ, but with the optimal range of values being offset depending on the curvature of the surface. Note that the scores are lower here than in the synthetic data, which can be attributed in part to the subjective nature of the manual segmentation. The global Jaccard scores (Eq. (16)) for each of the volumes are summarized in the bottom row of Fig. 6. Here we see a similar relationship between the optimized values of β and κ as observed in the localized scores and synthetic data. Examples of segmentations of all real images are provided in the supplementary material.

5.4.3 Comparison with other methods

Comparison of the curvature-enhanced random walker with other segmentation methods is summarised in Table 2. The curvature-enhanced random walker outperforms all other methods in terms of Jaccard scores, and measures of boundary error also show improvement in the curvature-enhanced random walker versus other methods. Fig. 7 shows this result in the context of an image (see also Supplementary Figure 12). The pixel classifier tends to have a low false negative rate but a high false positive rate, which manifests as an expanded boundary. The power watershed tends to be highly affected by noise, giving a rough boundary that can lead to large areas of false positives and large areas of false negatives. The random walker provides a smoother segmentation, but fails to accurately segment the protrusions, due to variation in intensity along these protrusions (see slices in Fig. 7). The curvature enhancement allows the recovery of these protrusions, leading to a more accurate segmenta-

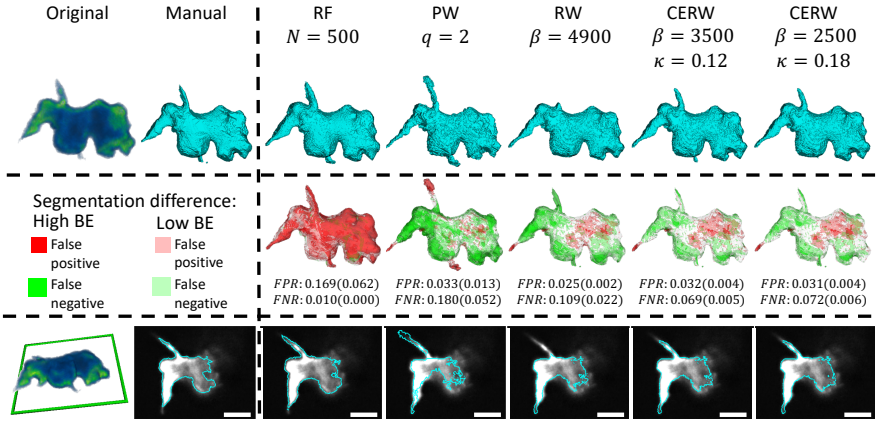

Figure 7: Comparison between manual segmentation and random forest classifier (RF), power watershed (PW), random walker (RW), and curvature-enhanced random walker (CERW). Top row: surfaces of each segmentation. Middle row: differences between segmentation results and manual segmentation, where red marks false positive, green marks false negative, and reduced opacity is given to pixels with a boundary error of 1 (low BE). FPR: false positive rate, FNR: false negative rate, numbers in brackets are error rates of high BE points only. Bottom row: slices through each surface compared to original image, scale bars represent 5 μm. The CERW outperforms all other methods, with almost all errors having low boundary error. Note a region is marked as false positive in all segmentations. This region could potentially be regarded as true positive (see bottom row), but the experimenter chose not to include it.

tion. Additionally, the false positive and false negative rates are much more balanced in the curvature-enhanced random walker than in the other methods, which suggests that it has less bias toward over- or under-segmenting the image.

6 Discussion

We have added a curvature term to the anisotropic diffusion representation of the random walker method. This yielded an improvement to the original random walker in both real cell images and synthetic data. Furthermore, this method performs better than the power watershed in both real and synthetic data, and the random forest pixel classifier in real data.

The main advantage of using the curvature-enhanced random walker over the standard random walker is the ability to recover finer details in the image. This is especially useful in microscopy images, where image capture tends to blur these finer features and deconvolution can only partially compensate for this effect.

Another advantage of the curvature-enhanced random walker over the standard random walker is that lower values of β can be used with a sufficiently large κ, which reduces the impact of noise on the segmentation. This is because, for low β and high κ, the effect of diffusion being weakly-linked to the image gradients is balanced by the curvature term enhancing the finer structural details, leading to smooth boundaries in the segmentation where

Method	JS	Local Jaccard			HD	BDE	
		H^-	H^0	H^+		S→GT	GT→S
RF (50)	0.783	0.632	0.741	0.684	12.6	1.96	1.38
RF (500)	0.835	0.700	0.798	0.734	9.33	1.35	0.896
PW (2)	0.849	0.769	0.800	0.699	10.5	1.13	0.867
RW (4900)	0.865	0.788	0.827	0.727	9.22	0.923	0.884
CERW $(4900, 0.06)$	**0.869**	**0.792**	0.837	0.763	**7.54**	**0.916**	**0.810**
CERW $(3500, 0.12)$	0.868	0.790	**0.838**	**0.764**	7.73	0.925	0.811
CERW $(2500, 0.18)$	0.868	0.790	0.837	0.761	8.06	0.923	0.821
CERW $(1500, 0.30)$	0.866	0.787	0.834	0.753	8.92	0.931	0.841
CERW $(1000, 0.50)$	0.863	0.780	0.831	0.751	9.51	0.962	0.848

Table 2: Comparison of segmentation methods applied to real data. RF: random forest classifier, PW: power watershed, RW: random walker, CERW: curvature-enhanced random walker. Numbers in brackets are parameter values (see text for details). JS: Jaccard score, Local Jaccard scores are separated into areas of negative curvature (H^-), low curvature (H^0), and positive curvature (H^+). HD: Hausdorff distance, BDE: mean boundary displacement error, measuring the displacement of the ground truth (manual segmentation) boundary compared to the segmentation boundary (GT→S), and the reverse (S→GT). Bold numbers highlight the best value (highest for Jaccard and local Jaccard, lowest for Hausdorff distance and boundary displacement error).

the curvature is low, but detailed feature recovery where the curvature is high. This effect is especially advantageous when analysing how the cell surface changes over time, since the segmentation surface is less prone to arbitrary noise-induced variations between time frames.

While we have not explicitly examined the stability of the curvature-enhanced random walker, our experiments show that there is a range of values of β and κ that produce stable results (see Figs 4 & 6). The only cases where we observed instability was for high β and high κ (top right in Fig. 6). In such instances, the system did not converge. This effect is likely due to the fact that the curvature enhancement is inherently unstable, and this instability is only mitigated by the diffusion term in Eq. 7. If β is large, then this reduces the rate of diffusion, which in turn reduces the stability of the system. The question of stability will be a topic of future research.

In the microscopy data, larger values of β are required to obtain the optimal segmentations than in the synthetic data. This could be due to the fact that while both real and synthetic datasets are normalized to $[0,1]$, the intensities of the cell membrane in the microscopy data are more variable than in the synthetic data, due to the fact that some areas show stronger fluorescence than others. This means that most of the boundary is of a reduced intensity, and requires a larger gradient coefficient to compensate for this effect.

The relationship between the optimal values of β and κ depends on the local curvature (Fig. 6). Specifically, areas of highly positive curvature require a larger value of κ than areas of highly negative curvature to attain the optimal Jaccard scores, although there is a small overlap in these optimal values. Additionally, areas of highly positive curvature have a lower Jaccard score than areas of highly negative curvature for the curvature-enhanced random walker (see Table 2). This is potentially due to the nature of the structures on the cell membrane that give rise to these curvature values; highly positive curvature corresponds to filopodia, which are long, thin protrusions on the cell membrane, while highly negative

curvature corresponds to macropinocytotic cups, which in our data were much wider than the filopodia and relatively shallow. This means that highly positive curvature is associated with sharper features than highly negative curvature, which suggests that the variation in κ is linked to the shape of the features being segmented, rather than the sign of the curvature of the surface.

We have only investigated the application of our method to single-cell images. The extension of the curvature-enhanced random walker to multi-cell images can be applied in a manner similar to previous random walker implementations [20]. For an image with N cells, given a seeding $\{S_i\}_{i=0}^{N}$ with S_0 representing background seeds, the distribution of v for the ith cell is computed by taking S_i as foreground and all other seeds as background seeds. The set of distributions $\{v_i\}_{i=0}^{N}$ are computed in parallel, with segmentation boundary for the ith cell given by

$$u_i = v_i - max_{j \neq i} v_j > 0. \tag{23}$$

The curvature term is computed for each i from the implicit isosurfaces of u_i, with the sign being determined by the sign of u_i.

7 Conclusion and future work

We have shown that our curvature-enhanced random walker segmentation method yields improvements on the standard random walker method, and performs better than other state of the art methods in real data. A relationship between the optimal weighting and curvature parameters is reflected in experiments on real and synthetic data. This relationship is subject to the shape of the objects being segmented and the intensity pattern of the data. Finer features in the data require a larger curvature coefficient in order to better resolve these features, while smaller (non-zero) curvature coefficients are preferable for larger features. There is an overlap between these optimal values given the data tested.

The methods presented here are based on a relatively simple formulation of the random walker and curvature enhancement. One possible extension could use a more elaborate weighting system, in a similar manner to M'hiri *et al.* [28]. Extensions in the curvature enhancement could include spatially varying κ, or using a formulation to increase the Willmore energy of implicit surfaces. The curvature enhancement presented here could also be applied to other methods, such as active contour segmentation, regularized by shape priors to reduce instability [23].

In terms of real data, we have only applied the curvature-enhanced random walker to 3D images of *Dictyostelium* undergoing macropinocytosis captured on an iSPIM light sheet microscope. This method would also be well-suited to segmenting other objects with complex surface structures, such as computed tomography images of vertebrae or lungs, or electron microscopy images of complex cell structures. Additionally, our method could easily be applied to 2D images, using curvature in place of mean curvature.

8 Acknowledgements

The authors thank Rob Kay and Peggy Paschke, MRC-LMB, for providing cell lines.

References

[1] Cédric Allène, Jean-Yves Audibert, Michel Couprie, Jean Cousty, and Renaud Keriven. Some links between min-cuts, optimal spanning forests and watersheds. *Mathematical Morphology and its Applications to Image and Signal Processing*, pages 253–264, 2007.

[2] Luis Alvarez, Pierre-Louis Lions, and Jean-Michel Morel. Image selective smoothing and edge detection by nonlinear diffusion. II. *SIAM Journal on Numerical Analysis*, 29 (3):845–866, 1992.

[3] Ignacio Arganda-Carreras, Verena Kaynig, Curtis Rueden, Kevin W Eliceiri, Johannes Schindelin, Albert Cardona, and H Sebastian Seung. Trainable weka segmentation: a machine learning tool for microscopy pixel classification. *Bioinformatics*, 33(15): 2424–2426, 2017.

[4] Serge Beucher and Fernand Meyer. The morphological approach to segmentation: The watershed transformation. *Mathematical Morphology in Image Processing*, 34:433–481, 1993.

[5] Yuri Y Boykov and M-P Jolly. Interactive graph cuts for optimal boundary & region segmentation of objects in nd images. In *Proceedings eighth IEEE International Conference on Computer Vision. ICCV 2001*, volume 1, pages 105–112. IEEE, 2001.

[6] Leo Breiman. Random forests. *Machine Learning*, 45(1):5–32, 2001.

[7] Vicent Caselles, Ron Kimmel, and Guillermo Sapiro. Geodesic active contours. *International Journal of Computer Vision*, 22(1):61–79, 1997.

[8] Nicholas D Condon, Adam A Wall, Jeremy C Yeo, Nicholas A Hamilton, and Jennifer L Stow. Image-based analysis of phagocytosis: Measuring engulfment and internalization. In *Phagocytosis and Phagosomes*, pages 201–214. Springer, 2017.

[9] Nicholas D Condon, John M Heddleston, Teng-Leong Chew, Lin Luo, Peter S McPherson, Maria S Ioannou, Louis Hodgson, Jennifer L Stow, and Adam A Wall. Macropinosome formation by tent pole ruffling in macrophages. *J Cell Biol*, 217(11): 3873–3885, 2018.

[10] Camille Couprie, Leo Grady, Laurent Najman, and Hugues Talbot. Power watershed: A unifying graph-based optimization framework. *IEEE transactions on pattern analysis and machine intelligence*, 33(7):1384–1399, 2010.

[11] Xingping Dong, Jianbing Shen, Ling Shao, and Luc Van Gool. Sub-markov random walk for image segmentation. *IEEE Transactions on Image Processing*, 25(2):516–527, 2015.

[12] Marc Droske and Martin Rumpf. A level set formulation for willmore flow. *Interfaces and Free Boundaries*, 6(3):361–378, 2004.

[13] Cheng-Jin Du, John G Ferguson, Phillip T Hawkins, Len R Stephens, and Till Bretschneider. Fast random walker for neutrophil cell segmentation in 3D. In *2012 9th IEEE International Symposium on Biomedical Imaging (ISBI)*, pages 190–193. IEEE, 2012.

[14] Noha El-Zehiry and Leo Grady. Optimization of weighted curvature for image segmentation. *arXiv preprint arXiv:1006.4175*, 2010.

[15] Noha Youssry El-Zehiry and Leo Grady. Contrast driven elastica for image segmentation. *IEEE Transactions on Image Processing*, 25(6):2508–2518, 2016.

[16] Selim Esedoglu, Andreas Rätz, and Matthias Röger. Colliding interfaces in old and new diffuse-interface approximations of willmore-flow. *arXiv preprint arXiv:1209.6531*, 2012.

[17] Alejandro F Frangi, Wiro J Niessen, Koen L Vincken, and Max A Viergever. Multiscale vessel enhancement filtering. In *International Conference on Medical Image Computing and Computer-Assisted Intervention*, pages 130–137. Springer, 1998.

[18] Jordi Freixenet, Xavier Muñoz, David Raba, Joan Martí, and Xavier Cufí. Yet another survey on image segmentation: Region and boundary information integration. In *European Conference on Computer Vision*, pages 408–422. Springer, 2002.

[19] Leo Grady. Multilabel random walker image segmentation using prior models. In *CVPR (1)*, pages 763–770. Citeseer, 2005.

[20] Leo Grady. Random walks for image segmentation. *IEEE Transactions on Pattern Analysis & Machine Intelligence*, 28(11):1768–1783, 2006.

[21] Michael Kass, Andrew Witkin, and Demetri Terzopoulos. Snakes: Active contour models. *International Journal of Computer Vision*, 1(4):321–331, 1988.

[22] Tae Hoon Kim, Kyoung Mu Lee, and Sang Uk Lee. Generative image segmentation using random walks with restart. In *European Conference on Computer Vision*, pages 264–275. Springer, 2008.

[23] L Kostrykin, C Schnörr, and K Rohr. Globally optimal segmentation of cell nuclei in fluorescence microscopy images using shape and intensity information. *Medical Image Analysis*, page 101536, 2019.

[24] Ernst Kuwert and Reiner Schätzle. Gradient flow for the willmore functional. *Communications in Analysis and Geometry*, 10(2):307–339, 2002.

[25] Wei Liao, Karl Rohr, and Stefan Wörz. Globally optimal curvature-regularized fast marching for vessel segmentation. In *International Conference on Medical Image Computing and Computer-Assisted Intervention*, pages 550–557. Springer, 2013.

[26] Jet Phey Lim and Paul A Gleeson. Macropinocytosis: an endocytic pathway for internalising large gulps. *Immunology and Cell Biology*, 89(8):836–843, 2011.

[27] Ravi Malladi and James A Sethian. Image processing via level set curvature flow. *Proceedings of the National Academy of Sciences*, 92(15):7046–7050, 1995.

[28] Faten M'hiri, Luc Duong, Christian Desrosiers, and Mohamed Cheriet. Vessel walker: Coronary arteries segmentation using random walks and hessian-based vesselness filter. In *2013 IEEE 10th International Symposium on Biomedical Imaging*, pages 918–921. IEEE, 2013.

[29] Neerad Phansalkar, Sumit More, Ashish Sabale, and Madhuri Joshi. Adaptive local thresholding for detection of nuclei in diversity stained cytology images. In *2011 International Conference on Communications and Signal Processing*, pages 218–220. IEEE, 2011.

[30] William Hadley Richardson. Bayesian-based iterative method of image restoration. *JOSA*, 62(1):55–59, 1972.

[31] Johannes Schindelin, Ignacio Arganda-Carreras, Erwin Frise, Verena Kaynig, Mark Longair, Tobias Pietzsch, Stephan Preibisch, Curtis Rueden, Stephan Saalfeld, Benjamin Schmid, et al. Fiji: an open-source platform for biological-image analysis. *Nature Methods*, 9(7):676, 2012.

[32] Jianhong Shen, Sung Ha Kang, and Tony F Chan. Euler's elastica and curvature-based inpainting. *SIAM Journal on Applied Mathematics*, 63(2):564–592, 2003.

[33] Ali Kemal Sinop and Leo Grady. A seeded image segmentation framework unifying graph cuts and random walker which yields a new algorithm. In *ICCV*, volume 1, page 3. Citeseer, 2007.

[34] Paul Wighton, Maryam Sadeghi, Tim K Lee, and M Stella Atkins. A fully automatic random walker segmentation for skin lesions in a supervised setting. In *International Conference on Medical Image Computing and Computer-Assisted Intervention*, pages 1108–1115. Springer, 2009.

[35] Yicong Wu, Alireza Ghitani, Ryan Christensen, Anthony Santella, Zhuo Du, Gary Rondeau, Zhirong Bao, Daniel Colón-Ramos, and Hari Shroff. Inverted selective plane illumination microscopy (iSPIM) enables coupled cell identity lineaging and neurodevelopmental imaging in *caenorhabditis elegans*. *Proceedings of the National Academy of Sciences*, 108(43):17708–17713, 2011.

[36] Jeremy Changyu Yeo, Adam Alexander Wall, Jennifer Lea Stow, and Nicholas Ahti Hamilton. High-throughput quantification of early stages of phagocytosis. *Biotechniques*, 55(3):115–124, 2013.

[37] Juyong Zhang, Jianmin Zheng, and Jianfei Cai. A diffusion approach to seeded image segmentation. In *2010 IEEE Computer Society Conference on Computer Vision and Pattern Recognition*, pages 2125–2132. IEEE, 2010.

[38] Pian Zhaoyu, Lu Pingping, Wu Lianxue, and Zhang Hong. A new image segmentation approach with structure tensor and random walk. In *2008 Second International Symposium on Intelligent Information Technology Application*, volume 2, pages 432–436. IEEE, 2008.